ACS APPLIED MATERIALS & INTERFACES

Research Article

www.acsami.org

In Situ Atomic Force Microscopy Study of Initial Solid Electrolyte Interphase Formation on Silicon Electrodes for Li-Ion Batteries

Anton Tokranov,[†] Brian W. Sheldon,*[,†] Chunzeng Li,[‡] Stephen Minne,[‡] and Xingcheng Xiao*[,§]

[†]Brown University - School of Engineering, 182 Hope Street, Box D, Providence, Rhode Island 02912, United States

[‡]Bruker Nano Surfaces, 112 Robin Hill Road, Goleta, California 93117, United States

[§]General Motors Global R&D Center, 30500 Mound Road, Warren, Michigan 48090, United States

ABSTRACT: Precise in situ atomic force microscopy (AFM) is used to monitor the formation of the solid electrolyte interphase (SEI) on Si electrodes. The stability of these passivation films on negative electrodes is critically important in rechargeable Li-ion batteries, and high capacity materials such as Si present substantial challenges because of the large volume changes that occur with Li insertion and removal. The results reported here show that the initial rapid SEI formation can be stabilized before significant Li insertion into the Si begins and that the rate at which this occurs varies significantly with the nature of the surface. The initial cycling conditions also have a substantial impact on the SEI that forms, with faster rates leading to a smoother, thinner SEI film. To quantitatively interpret the SEI measurements, irreversible expansion of the Si during the first cycle was also monitored in situ with specifically designed specimen configurations. On the basis of the experimental results, relatively simple models were also used to describe the initial formation and stabilization of the SEI and to describe the relationship between the SEI thickness and expected SEI degradation mechanisms.

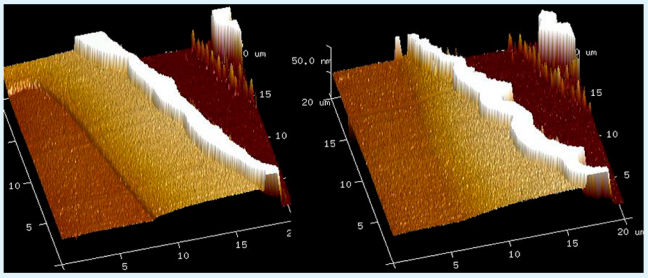

KEYWORDS: *solid electrolyte interphase (SEI), atomic force microscopy (AFM), Si anode, Li-ion battery*

1. INTRODUCTION

Much of the current research on rechargeable Li-ion batteries is motivated by electric vehicles, where improved energy density is critical. Silicon-containing anodes have received considerable attention, largely because pure Si has almost 10 times the capacity of the current commercial standard, graphite.[1] However, the corresponding large volume expansion that occurs during cycling can exceed 300%.[2,3] This creates substantial problems with mechanical degradation of the material that ultimately limits the cell lifetime. Recent research has begun to address these issues. For example, work on fracture mechanisms demonstrates that cracking can be reduced or eliminated by reducing size scales (e.g., employing nanosized particles, nanowires, etc.)[4−6] or by using a complex architecture.[7−13] Another serious difficulty associated with large volume changes is the formation of a stable passivation film on the electrode surface. Fundamental understanding of the formation and properties of these layers on Si has received less attention. The work presented here uses in situ measurements to probe the formation of these films.

The organic electrolytes that are widely used in Li-ion batteries are reduced on the anode surface to create a film that is usually referred to as the solid electrolyte interphase (SEI).[14] To prevent further electrolyte decomposition and the concomitant irreversible consumption of Li, this film must passivate the surface. This process and the passivation properties are critical because the Li loss to SEI formation ultimately reduces the capacity of the cell, a problem which is further exacerbated by the increase in relative surface area associated with the nanoscale Si materials that are widely studied. Stabilizing the SEI on Si is particularly challenging because the expansion of the electrode forces the SEI to expand, and this in turn can cause the SEI to break and reform, which greatly increases irreversible Li consumption and decreases lifetime. Some improvements in passivation have been achieved with artificial SEI layers,[15,16] encapsulation of Si particles,[17−19] electrolyte additives,[20−23] and combinations of several of these approaches.[24−28] The SEI chemistry and changes in the Si have been investigated with Raman spectroscopy,[29] XRD,[30] NMR,[31,32] and overall chemical composition.[33−35] Several previous papers have also reported in situ observations of SEI formation on Si, but these have been limited to electrochemical and impedance measurements[36−38] and recently in situ NMR.[39]

In the current paper, we investigate SEI formation at different potentials using in situ AFM measurements. By obtaining high spatial resolution in an electrochemical environment, we have been able to directly image the initial SEI formation process under different conditions. While there has been some previous AFM work done on battery electrodes, this has largely been focused on monitoring the expansion of patterned electrodes in situ[40,41] or ex situ,[42] on characterizing cracking,[43] or was based

Received: January 17, 2014
Accepted: March 26, 2014
Published: March 26, 2014

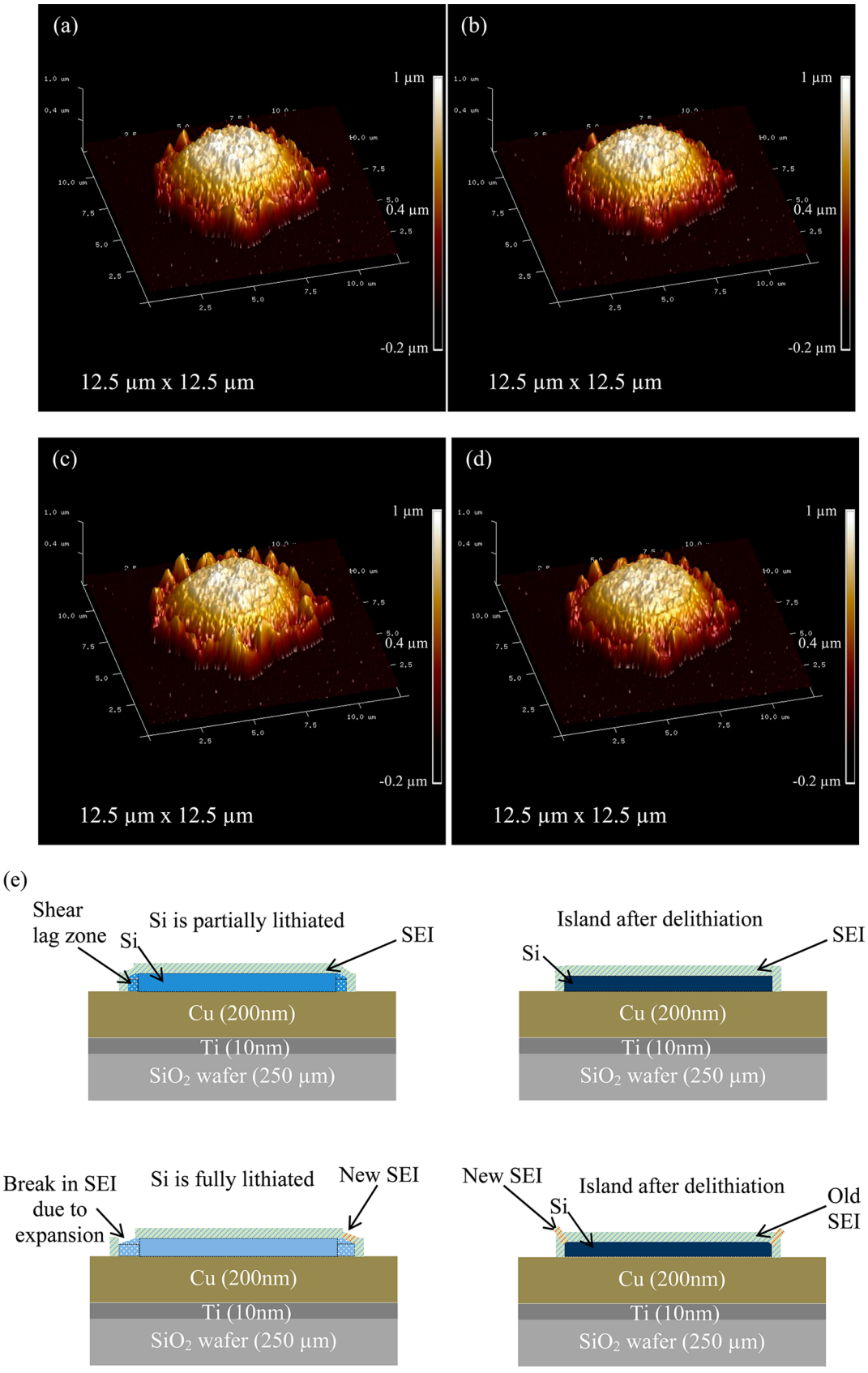

Figure 1. Si island after cycling to (a) 0.2 V, (b) 2.2 V, (c) 0.1 V, and (d) 2.2 V. In (a) and (b) the SEI is stable but is unable to withstand electrode expansion in (c) and shows irreversible SEI in (d). (e) Schematic diagram showing our interpretation of the results in (a)−(d).

on another material (e.g., carbon SEI[44,45] or tin SEI[46,47]). With the improved AFM instrumentation employed in our work, more precise measurements were possible. This allowed us to observe SEI formation in more detail than was previously

dx.doi.org/10.1021/am500363t | ACS Appl. Mater. Interfaces 2014, 6, 6672−6686

possible and provides useful information guiding the initial formation cycles to improve the long-term cycle stability.

While the configurations employed in our experiments facilitate precise AFM measurements, they clearly differ substantially from most battery electrodes. One critical difference in more realistic microstructures is the way that large Li-induced volume changes in Si produce large strains in the SEI. These effects are evident in our initial experiments (see Figure 1); however, most of the work presented here uses specimens that were specifically designed to prevent lateral expansion of the Si. This allowed us to focus attention on the underlying SEI formation mechanisms, in the absence of the large strains produced by volume changes in the Si. These findings are thus a necessary first step that serves as a basis for continuing work to build a detailed understanding of SEI formation in more complex Si structures.

2. EXPERIMENTAL APPROACH

The samples for the in situ AFM were prepared on 500 μm thick quartz wafers (40 mm diameter). A bonding layer of 10 nm thick Ti and 200 nm thick Cu current collector was deposited by electron beam evaporation, at a rate of 1 A/s for both metals. The island pattern was created by the lift-off process through a standard lithographic process, using the following procedure: Photoresist (AZ 5214 E) was spin coated on the current collector at 3000 rpm (500 rpm/s ramp rate) for a total time of 45 s. The prebake was at 110 °C for 60 s. The photoresist was exposed with 365 nm wavelength (80 mJ/cm^2 dose), using the nickel mesh (SPI Ni 500) as a photomask. The sample was then developed in AZ 300 MIF for 50 s. The deposition of Si was also done by the electron beam evaporation, with at least 8 h of pump down time (<2e-6 Torr) and at the deposition rate of 2 Å/s. Photoresist after the deposition was dissolved in acetone. The Al_2O_3 was deposited using reactive sputtering of aluminum in oxygen atmosphere. A 10% oxygen, 90% argon composition was used with an applied power of 180 W, resulting in a deposition rate of ~0.1 Å/s. For fabrication of Cu island samples the lithography procedure was identical, and Cu was deposited using the same technique as the current collector, followed by deposition of 5 nm thick Al_2O_3 as described above. For the complementary experiments done at Brown University, the only change was the wafer size which was 250 μm thick (25.4 mm diameter).

The in situ measurements were conducted with a Dimension ICON Electrochemical AFM setup inside an argon-filled glovebox (Nano Surfaces Division, Bruker), where both H_2O and O_2 were below 10 ppm. The tips used were FastScan-C (Bruker AFM Probes), composed of a silicon nitride cantilever with a sharp silicon tip. Cycling was conducted against Li metal foil, in an electrochemical cell designed for lithium-ion battery materials, and sealed during AFM operation. The electrolyte was a mixture of ethylene carbonate (EC) and dimethyl carbonate (DMC) (1:1 vol. ratio with 1 M $LiPF_6$). Constant voltage holds were used for most of the experiments, to permit more direct comparisons between samples.

The cycled samples were also examined with post-mortem transmission electron microscopy (TEM, JEOL 2100F). A focused ion-beam (FIB, FEI HELIOS 600) was used to prepare these specimens using a lift-out technique, to create a cross section of the cycled films.

3. RESULTS

3.1. Expansion and Contraction of Si Islands. An initial example of AFM observations during electrochemical cycling of a Si island is shown in Figure 1. The 46 nm film thickness here is significantly smaller than that used in previously reported AFM investigations of Si.[40,41] With this configuration, significant lateral expansion of the islands has been directly observed and attributed to shear lag effects.[48] In this prior work, the islands were produced by through-mask sputtering. In the current AFM study, the lithographically produced islands exhibit less lateral expansion. This difference appears to be caused by residual photoresist at the edge of the islands. In most of the experiments described below, this edge feature was large enough to prevent lateral motion (this simplifies the interpretation of some of the results). In Figure 1 there is less pinning due to the photoresist, and some lateral expansion is still observed. During the first cycle (partial lithiation to 0.2 V (Figure 1(a)) and subsequent delithiation (Figure 1(b)), the lateral expansion is due to both Si expansion and SEI formation. During the next cycle, the lower potential of 0.1 V produces more lateral expansion due to additional lithiation (Figure 1(c)). Here, a much larger irreversible out-of-plane expansion is observed near the island edge.

To interpret the large vertical expansion near the outer edges in Figure 1, it is first important to consider the implications of the shear lag region.[48,49] At a free edge, shear lag operates over a distance on the order of $h\sigma\tau^{-1}$, where σ is the in-plane stress in the center of the island and τ is the interfacial resistance to this lateral expansion (due to either plastic deformation in the current collector or sliding along the interface). In the absence of SEI considerations, the maximum out-of-plane expansion will occur in the center of these islands, while the lateral expansion in the shear lag region will reduce the out-of-plane expansion. In contrast to this the AFM results in Figure 1 show large expansion near the edges. We attribute this to unstable SEI formation in the shear lag region, as depicted in Figure 1(e). This does not occur in the center of the island where passivating SEI can form without lateral expansion of the underlying Si (i.e., where the Si behaves like a continuous film with expansion only occurring normal to the substrate). On the basis of this understanding, the irreversible lateral expansion during the first cycle reflects both Si expansion and some SEI formation on the edge. Note that during the first cycle to 0.2 V the SEI thicknesses in the edge and center of the island do not differ as dramatically as they do after the subsequent cycle to 0.1 V. In the subsequent cycle we believe that the large irreversible expansion near the edge reflects SEI which initially forms at higher potentials and then breaks open and continues to grow because of the larger lateral expansion of the island at lower potential. Here the behavior in the shear lag zone leads to both a large expansion parallel to the substrate during lithiation and a corresponding contraction during delithiation, and the latter appears to be masked by the large amount of SEI that forms during Li insertion. Thus, the SEI that initially forms at higher potentials is subjected to large lateral stresses when the underlying Si undergoes substantial lateral expansion in the shear lag region. In contrast, the Si closer to the center of the island is out of the shear lag zone, and here the Si expansion and contraction occur normal to the substrate. This absence of dimensional changes parallel to the SEI film leads to a much more stable SEI in the center of the islands. Since the AFM results only provide information on the change in dimensions, it is difficult to provide a precise interpretation of the differences that are observed near the edge of the island in Figure 1. However, it is noteworthy that the increase in thickness and roughness that occurs here is consistent with the idea of unstable SEI formation in the shear lag region.

Most of the subsequent investigation of SEI formation that is reported here focuses on Si islands where the shear lag effect is minimal (i.e., controlled with residual photoresist at the island edges). Note that the island configuration was used rather than

continuous films because this made it possible to use the surrounding Cu current collector as a reference for precise height measurements. The procedure for conducting baseline studies of SEI formation on Cu is described in Section 3.2, before proceeding to the presentation of the Si results in subsequent sections.

3.2. SEI on Copper. The growth of SEI on a Cu current collector provides a necessary reference measurement for the subsequent study of Si surfaces. The specimen configuration used for this is shown schematically in Figure 2(a). The oxide-coated islands were employed as a reference, with the AFM measuring the height difference. The dielectric film blocks electron conduction through the oxide such that there is no SEI growth on the pillar, and this then allows us to monitor SEI growth on the Cu as the difference between the two interfaces (Figure 2(b)). These results are shown in Figure 2(c), where most of the observed growth occurs during the hold at 1.5 V. We attribute this irreversible thickness change to the initial formation of SEI on Cu. Lithiation of the material is unlikely as Cu does not have significant capacity, and copper oxide does not have significant capacity above 1.5 V.[50,51] The quick stabilization of the thickness at 1.5 V suggests that continuing growth of this ~20 nm thick layer is much slower. This thickness is also maintained at the lower hold of 0.6 V, which indicates that the Cu surface is still passivated here. Some small thickness variations occur when the potential is dropped below 0.6 V; however, when the voltage is increased back to 1.5 V the thickness is again ~20 nm.

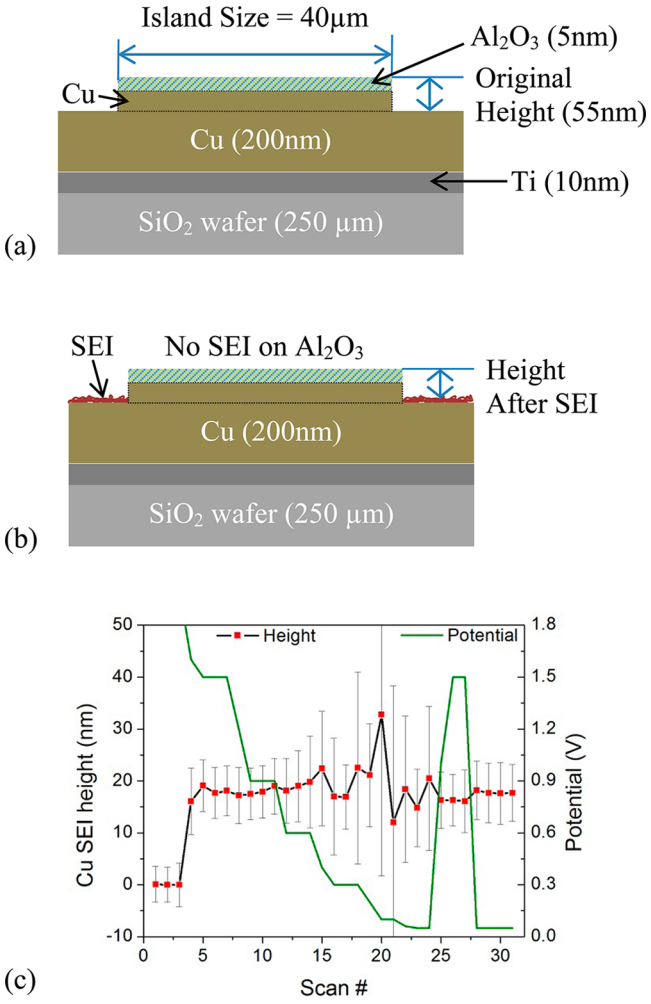

Figure 2. (a) Configuration for Cu SEI measurements, where original island height is approximately 55 nm. (b) After SEI growth the height difference decreases and is measured. (c) SEI thickness on Cu measured by AFM (orignal height − current height). Error bars show the average deviation.

There are several possible explanations for the small thickness increase that is observed at lower potentials (see Figure 2(c)). Some alloying between Li and copper oxide is known to occur, and this could explain the small reversible height change observed between 0.05 and 0.6 V. There is also evidence showing that a thin inorganic passivation layer forms at these voltages and that it forms at the bottom of the organic layer.[52] However, the change in height here is also close to the experimental limit for these measurements, and thus at this time it is difficult to determine the cause of this small reversible difference.

Overall, the AFM measurements on Cu are consistent with prior work on SEI formation. The SEI thickness observed here appears to be largely due to the organic decomposition products. The formation of a smaller amount of inorganic material may contribute some to the overall thickness at lower voltages; however, this is a much smaller effect and does not affect the measurements in the time frame of the experiment.

3.3. Simultaneous SEI Formation and Silicon Expansion. In prior work with Si it was observed that initial SEI consists primarily of organic decomposition products, followed by inorganic salts.[36] Based in part on this information, we used constant voltage holds, both above and below the potential where substantial Li insertion occurs in Si. Patterned Si islands were employed, such that the Cu current collector provided a convenient reference surface. At positions sufficiently far away from the edge of these islands, the Si surface behaves like a continuous thin film.[48] The AFM measurements were analyzed in two ways, by either looking at the average of the active area per scan (for the entire sample) or averaging each line individually to get higher resolution (single process).

Representative AFM images of a Si island at different states of charge are shown in Figure 3. The sample shows reversible cycling and no visible cracking or delamination during the timespan of the experiments. The irreversible height change observed after delithiation is attributed to both SEI formation and the a-Si phase transformation discussed in section 3.4. The tall feature at the edge of the islands is an artifact produced by the lithographic procedure employed during fabrication (described in Section 2). TEM shows that this edge contains residual photoresist, which appears to restrict the lateral motion of the islands along the metal surface. This stationary edge is seen in Figure 3 (in contrast to our previous work with islands produced by through-mask sputtering, where island edges exhibited significant lateral expansion).[48,49] Most of our subsequent experiments were conducted with specimens where more residual photoresist was present, to restrict the lateral expansion of the Si islands. This prevents the uncontrollable SEI formation seen near the edges in Figure 1 and allowed us to conduct detailed investigations of SEI formation on Si surfaces that only expand normal to the substrate. During electrochemical cycling, the displacement of the top surface of these Si islands is caused by both SEI formation and the Li-induced expansion of the underlying active film. The latter is expected to dominate when the voltage drops below 0.6 V. This is clearly observed in Figure 4(a)

dx.doi.org/10.1021/am500363t | ACS Appl. Mater. Interfaces 2014, 6, 6672−6686

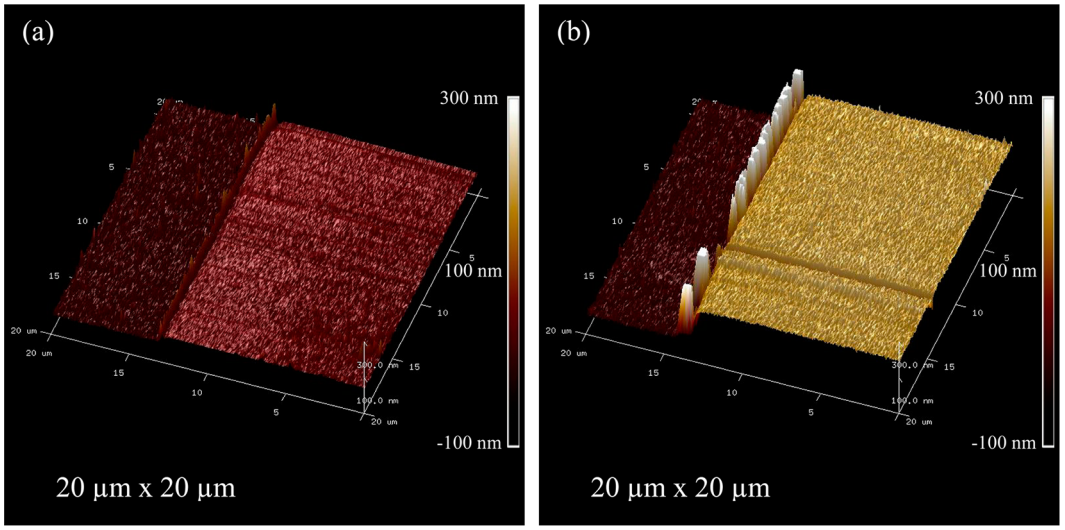

Figure 3. 3D image of electrode with the "pulse" SEI: (a) pristine electrode and (b) fully lithiated electrode during the 2nd cycle.

where the measured surface heights at the end of the 0.05 V hold were 220 nm (367%) and 200 nm (333%), at the island center and edge, respectively. At the end of this relatively short hold, the measured expansion is slowing, but it has not yet fully equilibrated (i.e., Li is still diffusing into the Si). In these measurements it is not possible to determine whether the SEI thickness is still increasing as the Si expands. However, after delithiation the net height change observed here is 80 nm (center) and 65 nm (edge). These are substantially thicker than the corresponding net change on Cu. Interpreting this AFM data further requires an assessment of the combined effects of SEI formation and irreversible Si expansion. The TEM image in Figure 4(c) confirms that the SEI layer is noticeably thicker than the corresponding ∼20 nm thick layer observed on Cu and that the rest of the height difference is caused by irreversible expansion of the Si. The EDS scan on the TEM cross-section shown in Figure 4(d) confirms that the darker layer does not contain Si and is thus SEI. These data also show significant Pt penetration in the SEI, which suggests that the layer is porous. This is also consistent with previously reported results.[52−55]

The results in Figure 4(a) also show that the island center expands more than the edges, throughout the process. Analogous thickness variations have been reported with thicker islands.[40] This center to edge height profile may be associated with the apparent phase boundary that exists between amorphous and lithiated Si during the first cycle,[56] although it is not yet clear that this argument is fully consistent with our experiments.

3.4. Silicon Coated with Aluminum Oxide. An additional investigation of irreversible Si expansion was conducted using an island coated with a 10 nm thick Al oxide film. This dielectric again blocks the transport of Li ions and electrons (i.e., similar to its effect on Cu described in Section 3.2). In these specimens, lithiation/delithiation occurred through edge defects that were produced during lithography (Figure 5(a)). This is seen in Figure 5(b) where a clearly discernible profile moves in from the edge. This is absent in the following cycles, as can be seen in Figure 5(c). The average height during cycling is plotted in Figure 5(d). The amounts of expansion during lithiation (180 nm) and after delithiation (70 nm) are both less than the analogous measurements on the island in Figure 4(a). This is consistent with the expected absence of SEI on top of the oxide. Also, the reversible expansion after delithiation is almost identical to that observed in the TEM image in Figure 4(c) (i.e., in the postcycled Si island). On the basis of these similar thicknesses, we conclude that the irreversible expansion in the Si is not particularly sensitive to the SEI layer that forms.

The direct AFM measurements on this specimen also made it possible to track the motion of the lithiation front. Since the lithium is inserted into Si through the edge, the scan in Figure 5(a,b) shows a sharp boundary between the lithiated and delithiated regions, which is consistent with other recent work where this type of sharp boundary was observed in amorphous Si during the first cycle.[56,57] The position of this front as a function of time is plotted in Figure 5(e). The initial time here corresponds to the point where the voltage is decreased from 0.3 to 0.1 V. A quantitative interpretation of the initial transient is difficult; however, after several minutes the interface moves at a rate of ∼4.7 nm/s. This type of front was not observed during delithiation, where the measured height drops uniformly. This is consistent with prior in situ TEM work which shows that the type of sharp boundary indicated in Figure 5(e) is only present during the initial lithiation cycle.

Most of the expansion at lower voltages is caused by lithiation of the Si, and the results in Figure 5(d) show that a substantial amount of this expansion is irreversible after the Li is removed. For comparison, recent observations with in situ TEM[56] show that after one full lithiation/delithiation cycle amorphous particles exhibit an increase in radius of ∼9.5%. This corresponds to a volume increase of ∼31%, which is reasonably close to our measured change of ∼15%. We believe that our observation provides important validation of this prior work. One important distinction is that the AFM cell permits the use of liquid electrolytes that are used in real batteries. The electrical contact is also better defined in the AFM cell, compared to the TEM where electrical contact with the nanostructured Si can be more difficult to maintain. Another difference is that the in situ TEM experiments require very high overpotentials because of the challenges associated with the experimental configuration. Because of these issues, it is possible that some of the irreversible expansion in the TEM experiments is associated with difficulties in removing all of the Li from the Si. In comparison, the AFM measurements provide

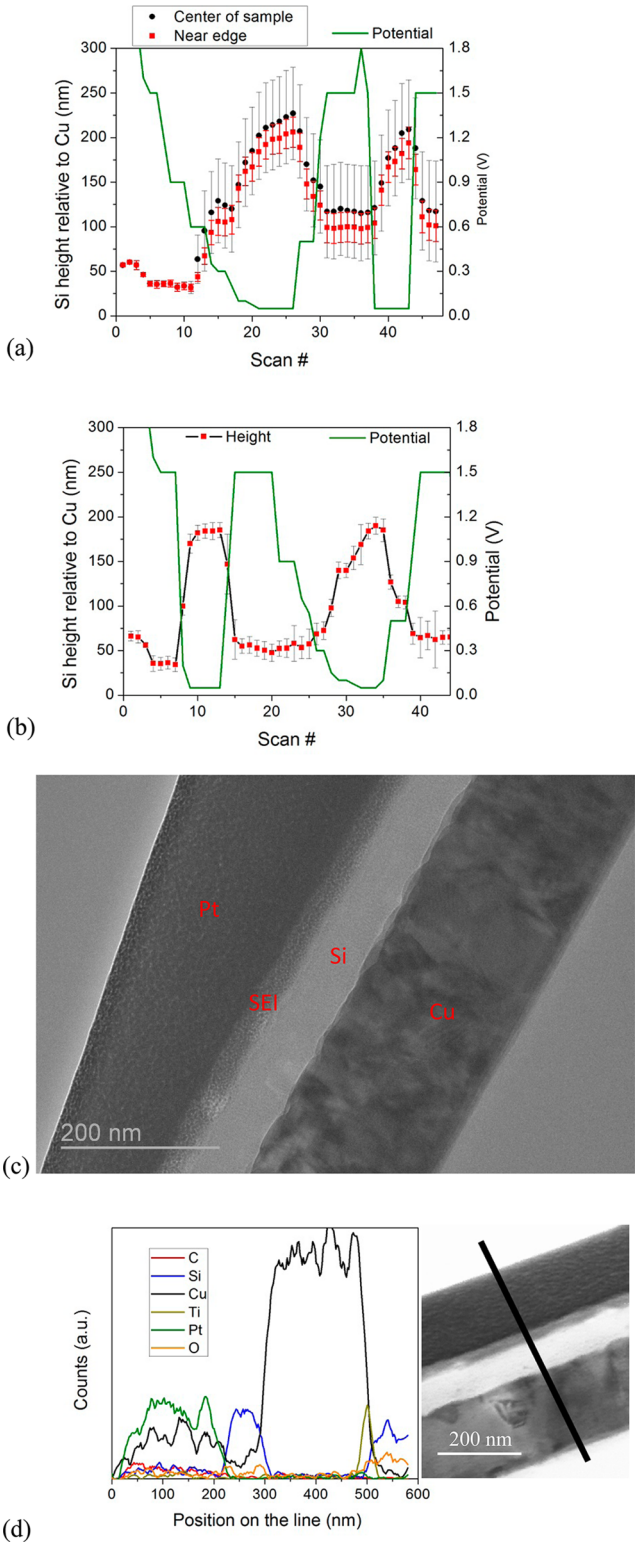

Figure 4. Height of Si electrode (error bars in a and b show the average deviation): (a) in situ AFM measurements during the slower first cycle, showing thick SEI formation; (b) in situ AFM measurements during the faster first cycle; (c) post mortem TEM image after the same cycling schedule as in part a; and (d) EDS of the cross-section (graph represents the intensity of elements along the line shown on the right).

much better voltage control, with excellent contact between the Si islands and the current collector throughout the experiments.

3.5. Surface Roughness. The AFM measurements also provide detailed information about the evolution of surface roughness. Comparisons between Cu and Si cycled under the same conditions are summarized in Table 1. On copper, the root mean squared (RMS) roughness increases during initial SEI formation and then reaches a fixed value. This parallels the growth of the SEI thickness that is occurring. The observation that the SEI is somewhat rougher than the initial Cu surface is consistent with expected inhomogeneities in the organic decomposition products (e.g., nanoporosity, etc.).

Much rougher surfaces were observed during SEI formation on Si. The RMS values here are comparable to or larger than the measured SEI thickness. One possible explanation is that the SEI that forms on Si is less homogeneous, possibly with more porosity. The large volume change and flow that occur in the underlying Si may also produce a rougher Si/SEI interface, which is then manifested in the rougher SEI/electrolyte interface observed by AFM. The reduced roughness observed near the edge of the Si islands may be related to the reduced out-of-plane expansion in the Si that also occurs near the edge (see Section 3.3). However, the transition to a smoother surface near the edge occurs rather abruptly. This difference could be related to the specimen preparation. Also, the amount of roughness detected by AFM is not immediately apparent in the TEM image in Figure 4(c). Because the AFM measurements are conducted in situ, they should reflect the surface that is present during electrochemical cycling. The preparations needed for TEM (drying, etc.) appear to reduce the roughness. This might, for example, be expected with a nanoporous layer.

3.6. Impact of Initial Cycling Conditions. The alternate conditions in Figure 4(b) were used to explore the impact of cycling rate. Here, the first cycle was conducted by quickly decreasing the voltage from 1.5 to 0.05 V, in contrast to the intermediate constant voltage holds employed with the specimens described in sections 3.2−3.5. These voltage holds were instead used in the second cycle. With this first cycle "pulse", the AFM measurements clearly show that the SEI is thinner. This is consistent with prior work showing that SEI formation at lower voltages can be more effective at passivating the surface against further SEI growth. The differences in SEI formed under different conditions are discussed further in Section 4. As noted in Section 3.3, initial Li insertion into the Si will contribute to the observed height increases. Looking at the reversible changes, both cycling conditions produce similar contractions of ∼100 nm during delithiation. This change is slightly larger in the "pulsed" sample, which may reflect some additional lithiation in this film (possibly due to slightly faster lithiation kinetics). The irreversible height change occurs mostly during the first cycle with ∼20 nm expansion during the pulse hold and another 10 nm during the second slower cycle. This is significantly less than the irreversible expansion measured during slower cycling.

For cycles with a rapid voltage drop from 1.5 to 0.05 V, the AFM measurements for different specimens are compared directly in Figure 6(a,b). The sample height was then calculated from each individual line scan to allow for resolution that is ∼5 s per data point. These results are consistent with the proposed interpretation of SEI formation. The fastest and largest expansion occurs when the pulse is used in the first cycle. With a subsequent pulse in the second cycle, the initial height is increased because of the pre-existing SEI from the first cycle. The total expansion due to Li insertion then reaches roughly the same height, which implies that minimal additional SEI

dx.doi.org/10.1021/am500363t | ACS Appl. Mater. Interfaces 2014, 6, 6672−6686

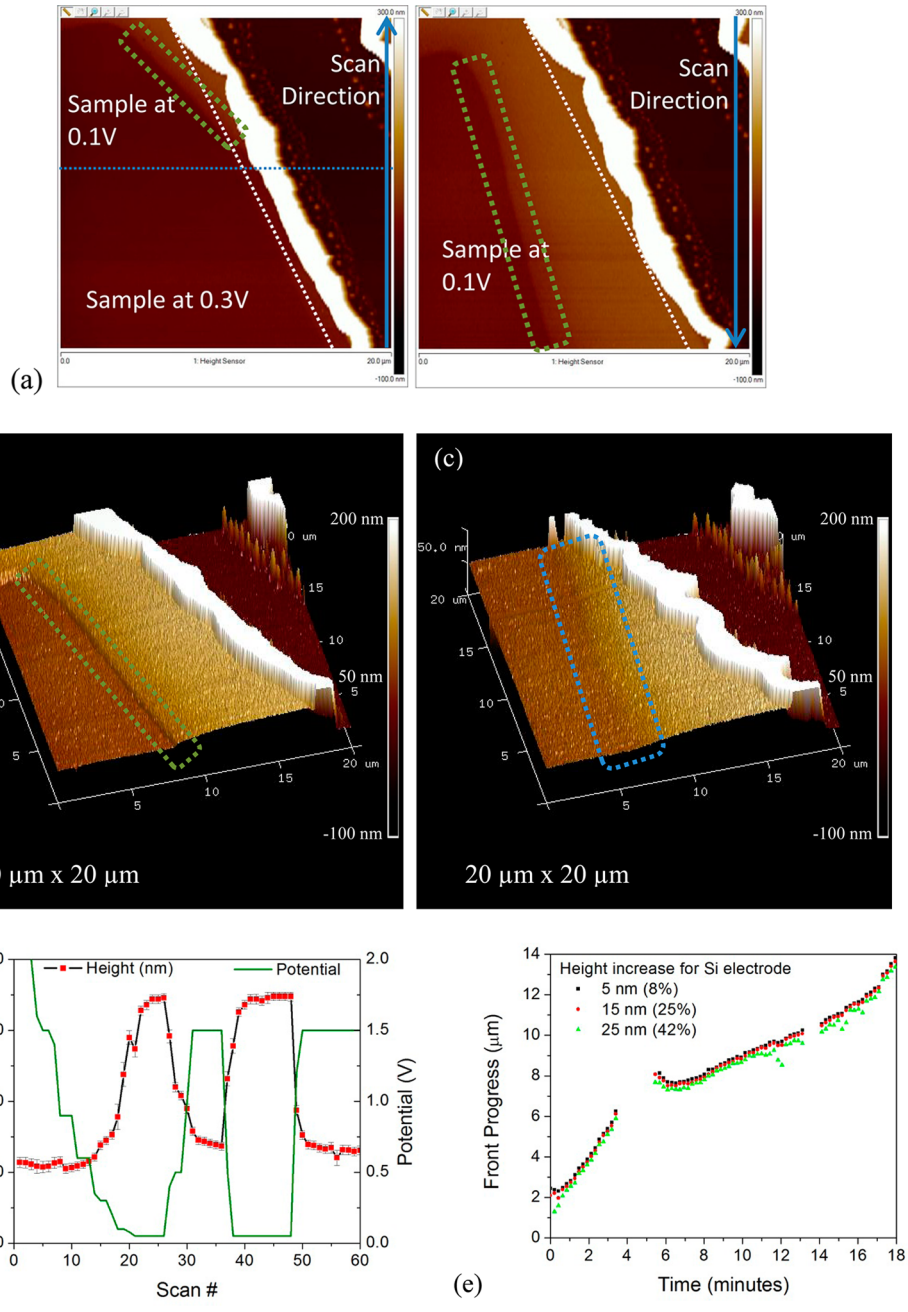

Figure 5. Al_2O_3 coated sample: (a) 2D image of the first cycle showing front motion (the front is surrounded by the green outline); (b) 3D image during the first cycle showing the front motion (the front is surrounded by the green outline); (c) 3D image of the Si during the second cycle (the area where the transformation was first seen in the first cycle is surrounded by the blue outline); (d) thickness plot; and (e) front progress relative to the edge. Multiple heights are shown to highlight the rapid transformation that is occurring.

Table 1. Surface Roughness of Cu and Si during Cycling

sample		RMS roughness (nm)			
		initial	after pulse	during full lithiation	after delithiation
Si island/ slower 1st cycle	Si center	5.7 (OCV)	N/A	64.8	66.6
	Si edge	4.1 (OCV)	N/A	20.3	20.6
	Cu	2.3 (OCV)	N/A	6.295	6.0
Si island/fast 1st cycle	Si	6.4 (air)	9.3	9.0	7.5
	Cu	3.9 (air)	10.0	9.2	7.9

growth occurs during this second cycle. The third data set in Figure 6(a) provides a fast second cycle that was run on a specimen where the first cycle was done with the 0.6 V hold described in Section 3.2 (i.e., slow cycling). The initial height is

dx.doi.org/10.1021/am500363t | ACS Appl. Mater. Interfaces 2014, 6, 6672−6686

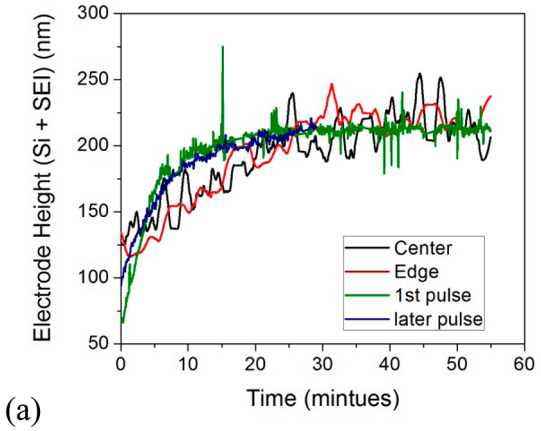

(a)

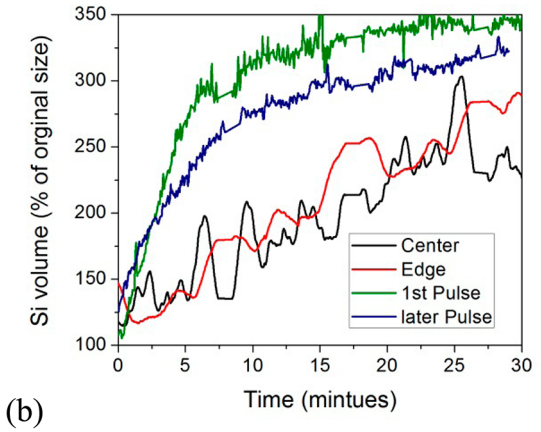

(b)

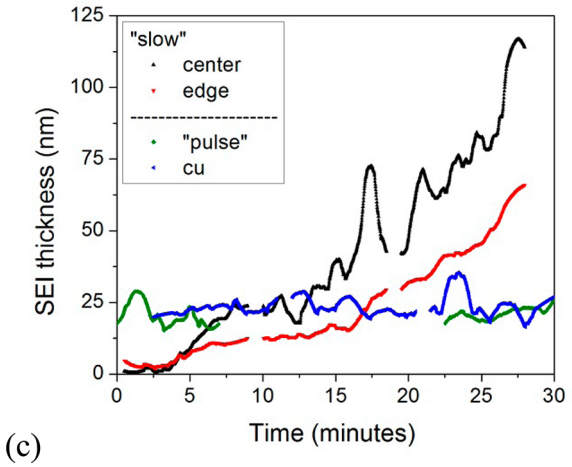

(c)

Figure 6. Change in electrode height due to various processes: (a),(b) SEI diffusion during fast lithiation (1.5 V → 50 mV voltage drop). (a) Electrode total height (Si + SEI height). (b) The expansion of the electrode relative to the electrode's original height (1st cycle irreversible expansion included). (c) SEI growth during 0.6 V holds. It can be seen that the SEI does not grow significantly on the Cu surface (after initial rapid formation) or after being exposed to lower potentials. Data smoothing was used for electrodes with thick SEI, due to surface roughness.

the largest of the three, which reflects the thicker SEI that forms during a slower first cycle. The somewhat slower rate of expansion that is shown in Figure 6(b) (during fast cycling) implies that this thicker SEI leads to an increased resistance to lithiation, under these conditions.

The thinner SEI formed with the first cycle "pulse" also exhibits significantly smaller RMS roughness values compared to the Si results presented in Section 3.5. Thus, the faster stabilization of the SEI that occurs here appears to be correlated with smoother SEI surfaces. This is generally consistent with the possible interpretations outlined in Section 3.5, to explain the differences observed between Si and Cu. Again, the roughness difference may reflect changes associated with the formation of the SEI/electrolyte interface and/or the SEI/Si interface.

4. ANALYSIS AND DISCUSSION

4.1. SEI Formation. Measured SEI growths at 0.6 V for different specimens are compared in Figure 6(c). On Cu a central observation is that the SEI layer reaches a relatively constant thickness quickly before 0.6 V. At this moderate potential, a thicker SEI forms at a somewhat slower rate on Si. Our interpretations of these results are largely based on the proposed mechanisms depicted schematically in Figure 7(a–c).

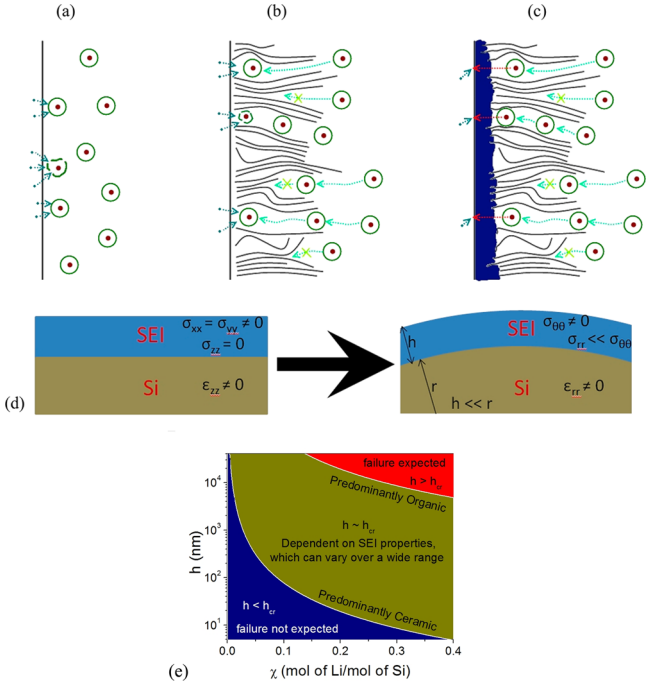

(d)

(e)

Figure 7. SEI growth model: (a) Formation of organic decomposition products at higher potential. (b) Continuing decomposition increases the SEI thickness and decreases mesoporosity, which reduces the growth rate as the solvation complex now has to diffuse to the electrode through SEI that is thicker and denser. (c) At lower voltage a dense SEI forms, which allows Li-ion diffusion but passivates by limiting both electrolyte diffusion and electrical conductivity. (d) Configurational differences between thin film and particle electrodes. (e) SEI failure limit based on SEI thickness, *h*, and estimated properties.

In part, these follow from prior work which shows that the first SEI constituents which form are organic decomposition products followed by inorganic components at lower potential (starting at ~0.3 V).[53] There have also been impedance studies of electrodes that observe poor passivation, increasing resistance in the upper voltage regime during the first cycle, but observed more conducting/passivating SEI at lower potential.[58,59] These reports are consistent with our observations, and from this it has been assumed that SEI created during

dx.doi.org/10.1021/am500363t | ACS Appl. Mater. Interfaces 2014, 6, 6672–6686

the 0.6 V holds is primarily organic. On Cu the SEI grows much more slowly after the initial rapid formation of a ~20 nm thick layer. It is not clear what limits further growth. In many materials, the growth of a dense passivation layer is often limited by diffusion. For SEI it has been argued that limited electron conduction should lead to this effect (shown schematically in Figure 7) since Li transport from the electrolyte must be relatively fast for a battery to function successfully.

One possible contributing factor to the slower initial SEI growth on Si is that slower electron conduction through the Si and its native oxide is likely to retard initial SEI formation. The first cycle measurements in Figure 6(c) show that the measured thickness continues to increase during the entire 0.6 V hold. This comparison confirms that the first cycle SEI formation process occurs relatively slowly.

After cycling to lower voltage and then delithiating, the net height difference clearly shows an irreversible expansion during the first cycle that is much larger than that observed on Cu. As noted in Section 3.3, this difference reflects both irreversible expansion of the Si and an SEI that is thicker than that observed on Cu. We propose two general explanations for this difference. One is that inherent chemical and/or structural differences in the Cu and Si surfaces lead to variations in the SEI structure that forms at or above 0.6 V. As one example, the faster initial growth observed on Cu might produce a denser structure which imposes a more stringent limit on subsequent growth. Again, the mechanisms outlined in Figure 7 provide possible explanations for how variations in the underlying electrode surface could lead to different SEI structures. A second significant difference between Cu and Si is that the latter undergoes a large expansion during lithiation. Because of this large volume change, the electrode/SEI interface is likely to be subjected to local fluctuations that may reduce the SEI stability. In a thin film, the simplest view is that expansion occurs only in one direction (normal to the electrode surface); however, even in this case variations in the surface profile during lithiation could lead to local perturbations that destabilize the SEI. While this interpretation is speculative at this point, this type of behavior warrants further investigation.

The experiments with rapid initial cycling (Section 3.6) provide additional insight into SEI formation and stability. Critical observations in this experiment are that thinner SEI forms during the rapid first cycle, and as already noted, it does not continue to grow in the second cycle during the 0.6 V hold (see Figure 7). This result is potentially consistent with the aforementioned previous work which proposes that improved passivation by the SEI is associated with processes that occur at lower potentials.[58,59] In the experiments with a rapid first cycle, this passivation should occur at a point where the SEI is thinner (i.e., compared to the first cycle with a 0.6 V hold). As noted above, the continuing increase in height during the first cycle 0.6 V hold in Figure 6(c) is likely to be caused by both SEI formation and initial slow lithiation of the underlying Si. However, this expansion is not observed after the first cycle pulse (i.e., during the second cycle 0.6 V hold shown in Figure 6(c)). This lack of expansion is consistent with an SEI layer that is stabilized after the first cycle pulse. This also indicates that there is no expansion occurring due to lithiation of the Si at these potentials. On the basis of this result, one can argue that the height increase at 0.6 V during the first cycle (Figure 6(c)) is due to SEI (organic compound), with minimal initial Li insertion in the underlying Si. This is consistent with the experiments, although it is also possible that the irreversible changes to the Si structure that occur during the first lithiation cycle will alter the initial stages of lithiation in later cycles (i.e., initial Li insertion could start at higher potentials during the first cycle).

The lithium transport properties are also very important for battery electrodes. The SEI resistance per unit length has been measured in other work and indicates that SEI formed at higher potential is more resistive.[53] This behavior combined with the increased thickness in our experiments suggests that SEI formed at higher potentials will negatively affect electrode cycling capability. This implies that faster Li ion transport will occur through the thinner SEI formed at lower potentials.

The SEI formed with rapid initial cycling is also smoother. It is possible that the organic layer that forms during the 0.6 V hold is inherently rougher only because it is thicker; however, the observed decrease in roughness with faster cycling may also reflect a smoother underlying Si surface. It is also possible that the stress state affects the SEI formation since during the "pulse" the electrode is in an expanded state which results in compressive stress on the SEI during delithiation. This requires further study, but as noted above a rougher Si/SEI interface could lead to less stable SEI, which in turn grows thicker (i.e., because of poorer passivation or more surface area). The simultaneous evolution of the interface structure as the SEI is forming suggests additional complexity in controlling the SEI properties. With reference to the specific experiments with Si that are reported here, this implies that faster cycling can lead to more stable SEI by limiting the disruption of the initial Si/SEI interface.

In general, it is convenient to describe SEI formation with passivation models that consider both reaction and diffusion mechanisms. To provide additional insight into the initial SEI formation that is tracked in the AFM experiments, we employ a relatively simple version of this approach. Relevant mechanisms here are the transport of electrolyte species to the electrode surface and electron conduction through the solid SEI constituents. The SEI growth rate (change in the thickness, h) due to both of these mechanisms can then be described with

$$\frac{dh}{dt} = \frac{V_m C^S}{\left[\frac{1}{k} + \frac{h}{D}\right]} + \frac{V_{m,el} C_{el}^S}{\left[\frac{1}{k_{el}} + \frac{h}{D_{el}}\right]} \quad (1)$$

where the el subscript refers to electron transport and the corresponding unsubscripted terms describe the mechanism based on electrolyte transport. The D's are then the relevant diffusivities, and the k's are generalized interface reaction rate constants (i.e., for a reaction that forms SEI at the electrode surface and at the SEI/electrolyte interface). More precise electrochemical descriptions of the interface reactions are clearly desirable, however, but given the limited scope of our current analysis a simple one-parameter description is sufficient. Other recent work has also employed the type of simple approach we use here.[60] The concentrations here refer to the respective species on the source side of the SEI (electrolyte surface for C^S and electrode surface for C_{el}^S). The molar volumes, V_m and $V_{m,el}$, describe the volume of SEI per mole of the respective species (electrolyte and electron).

Parabolic kinetics ($h \cong t^{1/2}$) have been observed during relatively long experiments with graphite electrodes.[61] This is often attributed to slow electron conduction through the passivation layer, behavior which is consistent with eq 1 at

longer times where electrolyte diffusion through the SEI ceases and the kinetics are dictated by a constant value of D_{el}. In contrast to this, we propose that the reactions that occur as SEI is first forming should be limited by electrolyte diffusion to the electrode surface. This process appears to correspond to the AFM measurements reported in Section 3, with a value of D that decreases rapidly during the formation of the initial layer. To describe this with eq 1, we employ a simple phenomenological form

$$D = D_o e^{-\alpha t} \tag{2}$$

Here D_o is taken to be roughly equal to the diffusivity of the rate-limiting decomposition species in the liquid electrolyte, and α describes the decrease in this diffusivity as the SEI structure evolves. The parameter α is dictated by the time-dependent evolution of the solid constituents in the SEI, including but not limited to the decrease in nanoporosity as the SEI becomes denser. More detailed modeling which describe these changes is certainly desirable; however, the form in eq 2 provides a convenient basis for interpreting the key observations in our experiments in terms of a single parameter, α. These assessments are summarized below.

4.1.1. Self-Limiting Initial SEI Growth. The premise that D_o corresponds to the liquid implies that $D_o \gg D_{el}$. Because D_{el} is relatively small, these effects are not readily apparent in our relatively short experiments (although these effects should dictate longer-term SEI growth). On the basis of this, we neglect the D_{el} term in eq 1 and analyze initial SEI formation with only the first term on the rhs and eq 2. This leads to a limiting thickness, $h \to h_\infty$ as $t \to \infty$:

$$h_\infty \sim \sqrt{\frac{2D_o V_m C^S}{\alpha}} - \frac{D_o}{k} \tag{3}$$

for relatively small values of D_o/k. This thickness corresponds to the state where electrolyte transport through the SEI is blocked (i.e., as $D_o e^{-\alpha t} \to 0$). Diffusion-controlled behavior corresponds to the first term on the rhs of eq 3, where fast interface kinetics make the last term negligible. With slower interface kinetics during initial SEI formation, the last term in eq 3 then predicts some reduction in the layer thickness (note also that as D_o/k increases more terms may be needed to accurately estimate h_∞).

4.1.2. Impact of the Initial Surface (Si vs Cu). The experimental results indicate slower SEI growth on Si, compared to Cu. This suggests a lower value of k. While the definition of k is relatively straightforward (at least in the basic model), in applying this description to the experiments the apparent value of k may also include effects of electron conduction in the underlying electrode (i.e., where slower conductivity in the Si leads to a lower effective k). In either case (slow interface reaction or low conductivity), the result in eq 3 indicates that a lower k for Si should reduce h_∞ (or have no apparent effect on this thickness if D_o/k is negligible for the relevant k's). There should also be a relationship between α and k. A more precise interpretation of the impact of interface reaction rates on α requires a better understanding of the internal structure of the SEI and its time-dependent evolution. However, a lower k should reduce the rate at which the SEI densifies and thus reduces α. An accurate mechanistic interpretation of this effect is difficult without additional data. As an example, note that if the SEI contains significant nanoporosity (suggested by the TEM observations in Figure 4) then a lower k should reduce the rate at which nanoporosity in the SEI is filled. As seen in eq 3, a lower value of α will lead to a thicker SEI that evolves over a longer time, which is also consistent with the experimental observations.

4.1.3. Thinner SEI with Faster Initial Cycling. The thinner SEI observed with the initial rapid drop to lower voltage is consistent with a larger value of α. This could reflect faster interface kinetics at low voltage and also a denser SEI that is associated with changes in the decomposition product (i.e., different phases, etc.). In this case, eq 3 predicts a thicker SEI with a higher value of k (i.e., with fixed α). Since this contradicts the experimental observations, we conclude that the dominant impact of faster cycling is a higher value of α, which reflects faster evolution of the internal SEI structure (and hence a smaller h_∞). In Section 3, we also noted that a smoother Si/SEI interface might contribute to the thinner SEI that was observed. While this is not captured directly in the 1D model that leads to eq 3, it is also possible to interpret local roughness effects in terms of their impact on the value of α (i.e., where roughness alters initial SEI formation in ways that tend to increase diffusivity and thus decrease α).

4.2. SEI Thickness and Stability. As described in Section 1, a critical issue in rechargeable batteries is the stability of SEI on electrodes with complex architectures. In these materials, the large volume changes in Si during cycling will produce additional large stresses in the SEI, in comparison with the patterned films employed in our investigation (e.g., see Figure 1). Configurational differences between our samples and simple particles are also shown schematically in Figure 7(d). The mechanical deformation that occurs in the SEI can be interpreted with a continuum mechanics framework, to evaluate stress evolution and failure. This is similar to recent work that analyzes failure mechanisms in core−shell structures.[62]

On the basis of our measurements we consider only stress-driven mechanisms in the initial SEI that forms (although the same concepts apply as the SEI becomes thicker during longer-term cycling). To demonstrate some of the key implications from our thickness measurements, the current analysis is limited to SEI with isotropic properties that deform elastically. The change in the underlying particle volume (V) with lithiation is also assumed to be isotropic

$$V(\chi) = V_o\left(1 + \frac{1}{V_m^o}\int_0^\chi \overline{V}_{Li} d\chi\right) \tag{4}$$

where χ is the Li content (moles Li per moles Si); V_o is the initial particle volume; V_m^o is the molar volume of the initial unlithiated Si; and the partial molar volume of Li in the active material, $\overline{V}_{Li}$, dictates the dimensional changes. For a spherical particle, the corresponding change in the particle radius R is then

$$R^2 dR = \frac{R_o^3}{3}\frac{\overline{V}_{Li}}{V_m^o} d\chi \tag{5}$$

where R_o is the initial radius. To simplify the current analysis, we also assume that the passivation layer is thin compared to the particle (i.e., $h \ll R_o$), which means that σ_{rr} is small and the hoop stress at the top of the film can be approximated with

$$\sigma_s(\chi) \cong \frac{M_s[\varepsilon_s^o + \overline{\varepsilon}_c(\chi)]}{\left[1 + h'\frac{(1+\nu+2m(1-2\nu_s))}{(1-\nu)}\right]} \tag{6}$$

dx.doi.org/10.1021/am500363t | ACS Appl. Mater. Interfaces 2014, 6, 6672−6686

where $h' = h/R_o$ and the value of σ_s decreases slightly at positions below the surface (i.e., eq 6 is the maximum value). Young's modulus and the Poisson ratio for the particle core and SEI are E, E_s, ν, and ν_s, respectively, and $m = E_s/E$. The biaxial modulus of the SEI is $M_s = E_s/[1 - \nu_s]$), and ε_s^o is defined as the strain in the passivation layer when $\chi = 0$ (i.e., due to intrinsic growth stresses in the SEI, etc.). For relatively small expansions the average linear expansion strain in the particle core is

$$\bar{\varepsilon}_c(\chi) \cong \frac{1}{3}\frac{\overline{V}_{Li}\chi}{V_m^o} \tag{7}$$

This result follows from eq 4 and the assumption that $\overline{V}_{Li}$ is independent of χ.[3] With $h \ll R_o$ the SEI is assumed to be too thin to provide any significant resistance to the expansion of the underlying Si (i.e., the SEI does not confine the underlying Si). Also the form of eq 7 is valid for relatively small strains, which only applies at relatively low lithiation levels (this is discussed further in conjunction with Figure 7(e) below). Combining eqs 6 and 7 describes the increase in tensile stress in the SEI as a function of the state of charge (i.e., χ). For the limiting case of very small h' this gives

$$\sigma_s(\chi) \cong M_s\left[\varepsilon_s^o + \frac{\overline{V}_{Li}\chi}{3V_m^o}\right] \tag{8}$$

As the SEI becomes somewhat thicker, the denominator in eq 6 shows that the stress will be smaller than the value in eq 8. On the basis of this, eq 8 is taken as an approximate upper bound. This provides a reasonable approximation for considering the failure mechanisms below, under the premise that we are considering SEI where h' is always significantly less than one. Note also that any mismatch in elastic properties is unlikely to substantially alter our analysis with eq 8, as long as the particle is as stiff or stiffer than the SEI (i.e., $m \leq 1$). Under these conditions, the second term in the denominator of eq 6 will be less than one (and usually much less than one).

4.2.1. SEI Thickness. Our in situ measurements provide direct information about the initial thickness of SEI films. The differences that were observed have implications for the mechanical stability of these layers since it is well-known that thicker films are more susceptible to failure. One important mechanism is through-thickness cracking. For the simplest case of a fully elastic SEI layer, basic fracture criteria lead to a critical thickness[63]

$$h_{cr}^f = \frac{2E_s\Gamma_f}{\pi c_e^2(1-\upsilon_s^2)\sigma_s^2} \tag{9}$$

(i.e., fracture is energetically favorable at $h > h_{cr}$), where Γ_f is the fracture energy of the SEI. The constant $c_e^2 = 1.26$, and the elastic response of the SEI is dictated by E_c (Young's modulus) and υ_c (Poisson ratio). This expression assumes that the film and underlying material have the same elastic properties. It is relatively straightforward to evaluate a mismatch in these properties,[63] but this level of detail is not included here, given the absence of precise information about the SEI properties. Interfacial debonding between an elastic SEI layer and an elastic substrate is also described with a similar critical value.[63]

$$h_{cr}^d = f_d E_c \frac{\Gamma_d}{\sigma_s^2} \tag{10}$$

where Γ_d is the interfacial delamination energy and f_d is a geometric factor that depends on the specific configuration (two standard cases are a straight delamination front where $f_d = 2/(1-\upsilon_s^2)$ and a circular pinhole where $f_d = (3+\upsilon_s^2)/(2(1-\upsilon_s^2))$). These debonding failures can be induced by either tensile or compressive stress (unlike the fracture criteria in eq 9), although buckling that leads to delamination is generally driven by compressive stresses. The result in eq 10 is again a limiting case where there is no elastic mismatch between the SEI and the particle.

Since the initial SEI films form quickly, we focus our attention on failures induced by the tensile stress that increases as the Si particle expands during Li insertion. Here, eqs 9 and 10 both show that the critical thickness decreases sharply with increasing σ_s (and hence increasing χ). Although these expressions are based on different failure mechanisms, it is convenient that the critical thickness values in eq 9 and 10 have similar forms

$$h_{cr}^i = \frac{\Gamma_i}{E_s}\frac{f_i}{[\varepsilon_s^o + \bar{\varepsilon}_c(\chi)]^2} \tag{11}$$

where the subscript i refers to one of the mechanisms in eq 9 and 10 (i.e., for fracture i corresponds to Γ_f and $f_f = 2/(\pi c_e^2(1-\upsilon_s^2))$, and for debonding i corresponds to Γ_d and f_d). For a given layer, the onset of mechanical failure is dictated by the mechanism with the smallest critical thickness, h_{cr}^{him}. This case defines the maximum strain where failures can be safely avoided. Since an SEI that only undergoes elastic deformation is restricted to relatively small strains, we treat only this case here. In this case, the maximum amount of Li that can be inserted in the Si particle, while maintaining an intact SEI film is given by:

$$\chi_{lim} \cong \frac{3V_m^o}{\overline{V}_{Li}}\left[\sqrt{\frac{\Gamma_{lim}}{E_s}\frac{f_{lim}}{h}} - \varepsilon_s^o\right] \tag{12}$$

Here, the subscript lim denotes the limiting failure mechanism. This expression can be used to interpret the impact of different SEI thicknesses. For example, the thinner SEI measured in the fast cycling experiments will increase χ_{lim} by ~40% (assuming that the SEI properties are identical for the two cases).

4.2.2. SEI Properties. Two important factors are not included in the basic analysis above. First, only elastic deformation in the SEI is considered. Other deformation processes could clearly lead to more damage-tolerant SEI, particularly in materials with a substantial organic content. Also, we assume that once the SEI forms it is inactive with respect to further lithiation/delithiation. Both of these effects will complicate the SEI response to changes in the underlying particle volume. With this in mind, the simpler analysis here is presented merely as a starting point for considering the stability of the initial SEI films that form. In this case, the mechanical properties that dictate behavior are limited to E_s, υ_s, Γ_f, and Γ_d. These have not been measured in SEI; however, the basic failure criteria outlined above provide some useful insight into the impact of these key quantities. In particular, from eq 10 note that Γ_{lim}/E_s is a critical quantity that will dictate failure during cycling.

To evaluate the impact of different Γ_{lim}/E_s values note that SEI is widely believed to contain a combination of inorganic and organic materials. Inorganic ceramics typically have values of $\Gamma_{lim}/E_s \sim 10^{-2}$–$10^0$ nm, whereas $\Gamma_{lim}/E_s \sim 10^1$–$10^4$ nm corresponds to the properties of many polymers and organics.[64]

Although these ranges reflect substantial variations in properties, it is instructive to use approximate values (0.1 nm for a typical ceramic and 100 nm for a typical polymer) in conjunction with eq 12 to define the regimes in Figure 7(e) (note that f_{lim} is of the order of 1 for the relevant mechanisms, and the initial strain in the SEI is neglected for these estimates). This comparison shows that at higher Γ_{lim}/E_s values (predominately ceramic), the initial SEI that forms on dense Si particles is only likely to survive with very small amounts of Li insertion in the underlying Si. Figure 7(e) also shows that moving to lower values of Γ_{lim}/E_s significantly increases the acceptable SEI thickness. This is largely due to the lower expected modulus values for polymers, which logically lead to much lower stresses in the SEI. Note here that the small strain approximation used to obtain eq 7 is reasonable for the limited composition range shown in Figure 7(e) but that a correction for larger strains is needed when the Si has a higher Li content.

4.2.3. Optimization of Initial SEI Formation. The basic failure criteria discussed above imply that optimizing the SEI is likely to involve minimizing h, minimizing E_s, and maximizing Γ_f and Γ_d. For example, both Figure 7(e) and the corresponding discussion above imply that damage-tolerant SEI will be obtained by maximizing Γ_{lim}/E_s. While this appears to suggest that organic SEIs are likely to be more successful, it is also important to note that the transport properties discussed in Section 3.2 will determine the thickness of the SEI, both during initial formation and during slower longer-term growth that we associated with D_{el} in eq 1. Here, we focus only on the initial SEI formation which was tracked in our experiments, where the value of α is critical in determining h_∞. Improved passivation properties (higher α) will lead to thinner SEI and improved failure resistance. On the basis of the analysis that leads to eq 12, the quantity to be maximized is

$$\phi \equiv \frac{f_{lim}}{\sqrt{2D_o V_m C^S}} \frac{\Gamma_{lim}\sqrt{\alpha}}{E_s} \tag{13}$$

This reflects the fact that a thinner film with significantly better passivating properties (higher α) can compensate for a lower Γ_{lim}/E_s value.

For single phase materials, each of the properties in eq 13 is either fixed or is likely to vary over a relatively small range. However, the complex SEI layers that have been observed usually consist of multiple phases. Thus, wide variations in specific properties are likely to be possible in these nanocomposite structures. Also, while the Si electrode properties clearly change with state of charge, it is not currently known whether any of the relevant SEI properties vary with the potential. Furthermore, the key kinetic parameter α is likely to depend on several more fundamental properties, in ways that have not yet been determined. Evaluating all of these properties in real SEI layers is an important challenge for ongoing research.

The lumped parameter in eq 13 applies only to the initial SEI formation process that was observed in our experiments. These measurements were apparently too short in duration to observe the slower growth of the SEI that is expected after a large number of cycles (i.e., the effect described with D_{el} in Section 4.1). At these longer times the basic failure mechanisms used to obtain eq 13 are still valid; however, additional SEI growth and passivation effects must be combined with the criteria in eq 11−13. This requires additional information about SEI growth, but in general these additional increases in the SEI thickness will promote failure by the mechanisms outlined above.

4.2.4. Other Experimental Observations: Irreversible Si Expansion and Surface Roughness. The estimates in Figure 7(e) are based on our first cycle results, where the SEI thickness is established before most of the lithiation occurs. This led to the assumption that $\varepsilon_c(\chi) \gg \varepsilon_s^o$. With full removal of Li from the Si, one might expect the volume expansion in eq 4 to be fully reversible; however, as already described in Section 3.4 this only occurs after the first cycle. When the initial SEI forms before significant lithiation of the Si (i.e., during the slow cycling experiments in Section 3), the irreversible first cycle expansion of the Si will lead to a relatively large value of ε_s^o at the end of the first cycle (i.e., residual tensile strain). For example, applying the measured volume change in Section 3.4 to spherical particles gives $\varepsilon_s^o \cong 0.15$. To describe the reversible volume changes and strains that are observed during subsequent cycling, a smaller value of $\overline{V_{Li}}$ should be used (i.e., in eq 4, etc.). This effect does not necessarily modify the criteria in Figure 7 after cycle 1 because AFM and other experiments show a consistent reversible expansion and contraction in subsequent cycles. Thus, applying the basic failure criteria in eq 9−11 would lead to essentially the same χ_{lim} value in the second and subsequent cycles.

As described above, the thinner SEI on Si observed after a faster voltage drop should improve failure resistance. The reduced surface roughness that was measured is also potentially advantageous. This is not immediately apparent in the failure criteria in eqs 9 and 10. Note here that the tensile failure limit in eq 9 assumes a limiting flaw size that is equal to the film thickness. This means that the result shown here is actually a lower limit, with the idea that highly uniform films can have a maximum flaw size that is less than the film thickness. In general a rougher film is likely to exhibit larger flaws and thus exhibit a critical thickness that is closer to the limit shown in eq 11. In general, roughness can lead to stress localization that promotes fracture and delamination.

5. CONCLUSIONS

In situ AFM measurements have provided new insight into the initial lithiation of Si electrodes. The key results are summarized as follows:

After the first lithiation/delithiation cycle, Si islands show a net increase in volume of ∼15% (i.e., they do not return to their original thickness).

During the first lithiation cycle, an initial SEI layer forms relatively quickly at 0.6 V on Si. Compared to a Cu film that was used as a reference, the formation rate on Si is slower, and the initial film that forms is thicker. A relatively simple model was developed to explain the limiting thickness of these layers, as a function of a single kinetic parameter α that phenomenologically describes electrolyte diffusion through the SEI.

Faster initial cycling leads to an SEI layer on Si that is thinner and smoother, even after subsequent cycling at slower rates. This indicates that the initial SEI structure is largely controlled by the conditions used in the first cycle.

The experimental observations with thin films were extended to consider the impact of initial SEI thickness on the stability of the layer that forms. For the simplified case of an elastic SEI film, a criteria for optimum SEI properties was defined with the single lumped parameter (eq 13).

Although the experimental results and analyses presented here are based on initial SEI formation, it is important to remember that the stability of SEI during long-term cycling is also critical. As noted in connection with eq 1, continuing growth after the initial SEI layer forms is likely to be limited by transport through the solid (probably the electron conductivity described with D_{el}). This longer term passivation behavior will depend, at least in some ways, on the initial SEI layer formation that we investigated. For example, cracking or delamination of the initial SEI will impact the morphology of the SEI that forms during subsequent cycling. The initial SEI structure will also dictate solid state transport properties and hence influence subsequent passivation, as seen in our results (although these effects could damp out after a large number of cycles). This type of trade-off is applicable to different materials where other mechanisms are operable—for example, the disruption of carbon surfaces by solvated ions during the initial stages of SEI formation could also lead to a more stable SEI.[65] In general, optimizing the SEI properties during initial electrochemical cycling will improve battery performance. More detailed evaluation of the correlations between initial SEI formation and longer term passivation behavior is an important area for continuing research.

AUTHOR INFORMATION

Corresponding Authors

*E-mail: brian_sheldon@brown.edu.

*E-mail: xingcheng.xiao@gm.com.

Author Contributions

The manuscript was written through contributions of all authors. All authors have given approval to the final version of the manuscript.

Notes

The authors declare no competing financial interest.

ACKNOWLEDGMENTS

This work was supported by GM-Brown Collaborative Research grant and NSF awards CMMI-1000822, DMR-0520651, and DMR-0805172. X.C.X. and B.W.S. also acknowledge the support by the Assistant Secretary for Energy Efficiency and Renewable Energy, Office of Vehicle Technologies of the U.S. Department of Energy under Contract No. DE-AC02-05CH11231, Subcontract No 7056410 under the Batteries for Advanced Transportation Technologies (BATT) Program. Financial support was provided in part by the US Department of Education through GAANN Award P200A090076, administered by the Institute for Molecular and Nanoscale Innovation at Brown University.

ABBREVIATIONS

SEI, solid electrolyte interphase; AFM, atomic force microscopy; RMS, root mean squared; EC, ethylene carbonate; DMC, dimethyl carbonate; TEM, transmission electron microscopy; FIB, focused ion-beam

REFERENCES

(1) Fleischauer, M. D.; Hatchard, T. D.; Bonakdarpour, A.; Dahn, J. R. Combinatorial Investigations of Advanced Li-Ion Rechargeable Battery Electrode Materials. *Meas. Sci. Technol.* **2005**, *16*, 212−220.

(2) Zhang, W.-J. A Review of the Electrochemical Performance of Alloy Anodes for Lithium-Ion Batteries. *J. Power Sources* **2011**, *196*, 13−24.

(3) Obrovac, M. N.; Christensen, L.; Le, D. B.; Dahn, J. R. Alloy Design for Lithium-Ion Battery Anodes. *J. Electrochem. Soc.* **2007**, *154*, A849−A855.

(4) Liu, X. H.; Zhong, L.; Huang, S.; Mao, S. X.; Zhu, T.; Huang, J. Y. Size-Dependent Fracture of Silicon During Lithiation. *ACS Nano* **2012**, *6*, 1522−1531.

(5) Chan, C. K.; Peng, H.; Liu, G.; McIlwrath, K.; Zhang, X. F.; Huggins, R. A.; Cui, Y. High-Performance Lithium Battery Anodes Using Silicon Nanowires. *Nat. Nanotechnol.* **2008**, *3*, 31−35.

(6) Chockla, A.; Bogart, T.; Hessel, C.; Klavetter, K.; Mullins, C.; Korgel, B. Influences of Gold, Binder and Electrolyte on Silicon Nanowire Performance in Li-Ion Batteries. *J. Phys. Chem.* **2012**, *116*, 18079−18086.

(7) Gohier, A.; Laïk, B.; Kim, K.-H.; Maurice, J.-L.; Pereira-Ramos, J.-P.; Cojocaru, C. S.; Van Tran, P. High-Rate Capability Silicon Decorated Vertically Aligned Carbon Nanotubes for Li-Ion Batteries. *Adv. Mater.* **2012**, *24*, 2592−2597.

(8) Zhang, C.; Gu, L.; Kaskhedikar, N.; Cui, G.; Maier, J. Preparation of Silicon@silicon Oxide Core-Shell Nanowires from Silica Precursor towards High Energy Density Li-Ion Battery Anode. *ACS Appl. Mater. Interfaces* **2013**, *5*, 12340−12345.

(9) Zhou, X.; Cao, A.-M.; Wan, L.-J.; Guo, Y.-G. Spin-Coated Silicon Nanoparticle/graphene Electrode as a Binder-Free Anode for High-Performance Lithium-Ion Batteries. *Nano Res.* **2012**, *5*, 845−853.

(10) Zhao, Y.; Liu, X.; Li, H.; Zhai, T.; Zhou, H. Hierarchical Micro/nano Porous Silicon Li-Ion Battery Anodes. *Chem. Commun.* **2012**, *48*, 5079−5081.

(11) Zhu, J.; Gladden, C.; Liu, N.; Cui, Y.; Zhang, X. Nanoporous Silicon Networks as Anodes for Lithium Ion Batteries. *Phys. Chem. Chem. Phys.* **2013**, *15*, 440−443.

(12) Gowda, S. R.; Pushparaj, V.; Herle, S.; Girishkumar, G.; Gordon, J. G.; Gullapalli, H.; Zhan, X.; Ajayan, P. M.; Reddy, A. L. M. Three-Dimensionally Engineered Porous Silicon Electrodes for Li Ion Batteries. *Nano Lett.* **2012**, *12*, 6060−6065.

(13) Park, M.-H.; Kim, M. G.; Joo, J.; Kim, K.; Kim, J.; Ahn, S.; Cui, Y.; Cho, J. Silicon Nanotube Battery Anodes. *Nano Lett.* **2009**, *9*, 3844−3847.

(14) Peled, E. The Electrochemical Behavior of Alkali and Alkaline Earth Metals in Nonaqueous Battery Systems—The Solid Electrolyte Interphase Model. *J. Electrochem. Soc.* **1979**, *126*, 2047−2051.

(15) Abel, P. R.; Lin, Y.-M.; Celio, H.; Heller, A.; Mullins, C. B. Improving the Stability of Nanostructured Silicon Thin Film Lithium-Ion Battery Anodes through Their Controlled Oxidation. *ACS Nano* **2012**, *6*, 2506−2516.

(16) Xiao, X.; Lu, P.; Ahn, D. Ultrathin Multifunctional Oxide Coatings for Lithium Ion Batteries. *Adv. Mater.* **2011**, *23*, 3911−3915.

(17) Wu, H.; Zheng, G.; Liu, N.; Carney, T. J.; Yang, Y.; Cui, Y. Engineering Empty Space between Si Nanoparticles for Lithium-Ion Battery Anodes. *Nano Lett.* **2012**, *12*, 904−909.

(18) Liu, N.; Wu, H.; McDowell, M. T.; Yao, Y.; Wang, C.; Cui, Y. A Yolk-Shell Design for Stabilized and Scalable Li-Ion Battery Alloy Anodes. *Nano Lett.* **2012**, *12*, 3315−3321.

(19) Luo, J.; Zhao, X.; Wu, J.; Jang, H. D.; Kung, H. H.; Huang, J. Crumpled Graphene-Encapsulated Si Nanoparticles for Lithium Ion Battery Anodes. *J. Phys. Chem. Lett.* **2012**, *3*, 1824−1829.

(20) Dalavi, S.; Guduru, P.; Lucht, B. L. Performance Enhancing Electrolyte Additives for Lithium Ion Batteries with Silicon Anodes. *J. Electrochem. Soc.* **2012**, *159*, A642−A646.

(21) Etacheri, V.; Haik, O.; Goffer, Y.; Roberts, G. A.; Stefan, I. C.; Fasching, R.; Aurbach, D. Effect of Fluoroethylene Carbonate (FEC) on the Performance and Surface Chemistry of Si-Nanowire Li-Ion Battery Anodes. *Langmuir* **2012**, *28*, 965−976.

(22) Lin, Y.-M.; Klavetter, K. C.; Abel, P. R.; Davy, N. C.; Snider, J. L.; Heller, A.; Mullins, C. B. High Performance Silicon Nanoparticle Anode in Fluoroethylene Carbonate-Based Electrolyte for Li-Ion Batteries. *Chem. Commun.* **2012**, *48*, 7268−7270.

(23) Elazari, R.; Salitra, G.; Gershinsky, G.; Garsuch, A.; Panchenko, A.; Aurbach, D. Li Ion Cells Comprising Lithiated Columnar Silicon Film Anodes, TiS2 Cathodes and Fluoroethyene Carbonate (FEC) as

a Critically Important Component. *J. Electrochem. Soc.* **2012**, *159*, A1440−A1445.
(24) Wu, H.; Yu, G.; Pan, L.; Liu, N.; McDowell, M. T.; Bao, Z.; Cui, Y. Stable Li-Ion Battery Anodes by in-Situ Polymerization of Conducting Hydrogel to Conformally Coat Silicon Nanoparticles. *Nat. Commun.* **2013**, *4*, 1943.
(25) Chen, X.; Li, X.; Ding, F.; Xu, W.; Xiao, J.; Cao, Y.; Meduri, P.; Liu, J.; Graff, G. L.; Zhang, J.-G. Conductive Rigid Skeleton Supported Silicon as High-Performance Li-Ion Battery Anodes. *Nano Lett.* **2012**, *12*, 4124−4130.
(26) Wu, H.; Chan, G.; Choi, J. W.; Ryu, I.; Yao, Y.; McDowell, M. T.; Lee, S. W.; Jackson, A.; Yang, Y.; Hu, L.; et al. Stable Cycling of Double-Walled Silicon Nanotube Battery Anodes through Solid-Electrolyte Interphase Control. *Nat. Nanotechnol.* **2012**, *7*, 310−315.
(27) Wu, X.-L.; Guo, Y.-G.; Wan, L.-J. Rational Design of Anode Materials Based on Group IVA Elements (Si, Ge, and Sn) for Lithium-Ion Batteries. *Chem.—Asian J.* **2013**, *8*, 1948−1958.
(28) Hu, Y.-S.; Demir-Cakan, R.; Titirici, M.-M.; Müller, J.-O.; Schlögl, R.; Antonietti, M.; Maier, J. Superior Storage Performance of a Si@SiOx/C Nanocomposite as Anode Material for Lithium-Ion Batteries. *Angew. Chem., Int. Ed. Engl.* **2008**, *47*, 1645−1649.
(29) Nanda, J.; Datta, M. K.; Remillard, J. T.; O'Neill, A.; Kumta, P. N. In Situ Raman Microscopy during Discharge of a High Capacity Silicon−carbon Composite Li-Ion Battery Negative Electrode. *Electrochem. Commun.* **2009**, *11*, 235−237.
(30) Hatchard, T. D.; Dahn, J. R. In Situ XRD and Electrochemical Study of the Reaction of Lithium with Amorphous Silicon. *J. Electrochem. Soc.* **2004**, *151*, A838.
(31) Key, B.; Bhattacharyya, R.; Morcrette, M.; Seznéc, V.; Tarascon, J.-M.; Grey, C. P. Real-Time NMR Investigations of Structural Changes in Silicon Electrodes for Lithium-Ion Batteries. *J. Am. Chem. Soc.* **2009**, *131*, 9239−9249.
(32) Trill, J.-H.; Tao, C.; Winter, M.; Passerini, S.; Eckert, H. NMR Investigations on the Lithiation and Delithiation of Nanosilicon-Based Anodes for Li-Ion Batteries. *J. Solid State Electrochem.* **2010**, *15*, 349−356.
(33) Pereira-Nabais, C.; Światowska, J.; Chagnes, A.; Ozanam, F.; Gohier, A.; Tran-Van, P.; Cojocaru, C.-S.; Cassir, M.; Marcus, P. Interphase Chemistry of Si Electrodes Used as Anodes in Li-Ion Batteries. *Appl. Surf. Sci.* **2013**, *266*, 5−16.
(34) Nie, M.; Abraham, D. P.; Chen, Y.; Bose, A.; Lucht, B. L. Silicon Solid Electrolyte Interphase (SEI) of Lithium Ion Battery Characterized by Microscopy and Spectroscopy. *J. Phys. Chem. C* **2013**, *117*, 13403−13412.
(35) Philippe, B.; Dedryvére, R.; Gorgoi, M.; Rensmo, H.; Gonbeau, D.; Edström, K. Role of the LiPF6 Salt for the Long-Term Stability of Silicon Electrodes in Li-Ion Batteries−A Photoelectron Spectroscopy Study. *Chem. Mater.* **2013**, *25*, 394−404.
(36) Lee, Y. M.; Lee, J. Y.; Shim, H.-T.; Lee, J. K.; Park, J.-K. SEI Layer Formation on Amorphous Si Thin Electrode during Precycling. *J. Electrochem. Soc.* **2007**, *154*, A515.
(37) Nadimpalli, S. P. V.; Sethuraman, V. A.; Dalavi, S.; Lucht, B.; Chon, M. J.; Shenoy, V. B.; Guduru, P. R. Quantifying Capacity Loss due to Solid-Electrolyte-Interphase Layer Formation on Silicon Negative Electrodes in Lithium-Ion Batteries. *J. Power Sources* **2012**, *215*, 145−151.
(38) Mazouzi, D.; Delpuech, N.; Oumellal, Y.; Gauthier, M.; Cerbelaud, M.; Gaubicher, J.; Dupré, N.; Moreau, P.; Guyomard, D.; Roué, L.; et al. New Insights into the Silicon-Based Electrode's Irreversibility along Cycle Life through Simple Gravimetric Method. *J. Power Sources* **2012**, *220*, 180−184.
(39) Delpuech, N.; Dupré, N.; Mazouzi, D.; Gaubicher, J.; Moreau, P.; Bridel, J. S.; Guyomard, D.; Lestriez, B. Correlation between Irreversible Capacity and Electrolyte Solvents Degradation Probed by NMR in Si-Based Negative Electrode of Li-Ion Cell. *Electrochem. Commun.* **2013**, *33*, 72−75.
(40) Beaulieu, L. Y.; Hatchard, T. D.; Bonakdarpour, A.; Fleischauer, M. D.; Dahn, J. R. Reaction of Li with Alloy Thin Films Studied by In Situ AFM. *J. Electrochem. Soc.* **2003**, *150*, A1457−A1464.
(41) Becker, C. R.; Strawhecker, K. E.; McAllister, Q. P.; Lundgren, C. A. In Situ Atomic Force Microscopy of Lithiation and Delithiation of Silicon Nanostructures for Lithium Ion Batteries. *ACS Nano* **2013**, *7*, 9173−9182.
(42) He, Y.; Yu, X.; Li, G.; Wang, R.; Li, H.; Wang, Y.; Gao, H.; Huang, X. Shape Evolution of Patterned Amorphous and Polycrystalline Silicon Microarray Thin Film Electrodes Caused by Lithium Insertion and Extraction. *J. Power Sources* **2012**, *216*, 131−138.
(43) Beaulieu, L. Y.; Eberman, K. W.; Turner, R. L.; Krause, L. J.; Dahn, J. R. Colossal Reversible Volume Changes in Lithium Alloys. *Electrochem. Solid-State Lett.* **2001**, *4*, A137−A140.
(44) Jeong, S.-K.; Inaba, M.; Abe, T.; Ogumi, Z. Surface Film Formation on Graphite Negative Electrode in Lithium-Ion Batteries: AFM Study in an Ethylene Carbonate-Based Solution. *J. Electrochem. Soc.* **2001**, *148*, A989−A993.
(45) Jeong, S.-K.; Inaba, M.; Iriyama, Y.; Abe, T.; Ogumi, Z. Surface Film Formation on a Graphite Negative Electrode in Lithium-Ion Batteries: AFM Study on the Effects of Co-Solvents in Ethylene Carbonate-Based Solutions. *Electrochim. Acta* **2002**, *47*, 1975−1982.
(46) Lucas, I. T.; Pollak, E.; Kostecki, R. In Situ AFM Studies of SEI Formation at a Sn Electrode. *Electrochem. Commun.* **2009**, *11*, 2157−2160.
(47) Tian, Y.; Timmons, A.; Dahn, J. R. In Situ AFM Measurements of the Expansion of Nanostructured Sn−Co−C Films Reacting with Lithium. *J. Electrochem. Soc.* **2009**, *156*, A187−A191.
(48) Soni, S. K.; Sheldon, B. W.; Xiao, X.; Verbrugge, M. W.; Ahn, D.; Haftbaradaran, H.; Gao, H. Stress Mitigation during the Lithiation of Patterned Amorphous Si Islands. *J. Electrochem. Soc.* **2012**, *159*, A38−A43.
(49) Haftbaradaran, H.; Xiao, X.; Verbrugge, M. W.; Gao, H. Method to Deduce the Critical Size for Interfacial Delamination of Patterned Electrode Structures and Application to Lithiation of Thin-Film Silicon Islands. *J. Power Sources* **2012**, *206*, 357−366.
(50) Grugeon, S.; Laruelle, S.; Herrera-Urbina, R.; Dupont, L.; Poizot, P.; Tarascon, J.-M. Particle Size Effects on the Electrochemical Performance of Copper Oxides toward Lithium. *J. Electrochem. Soc.* **2001**, *148*, A285−A292.
(51) Gao, X.; Bao, J.; Pan, G.; Zhy, H.; Huang, P.; Wu, F.; Song, D. Preparation and Electrochemical Performance of Polycrystalline and Single Crystalline CuO Nanorods as Anode Materials for Li Ion Battery. *J. Phys. Chem.* **2004**, *108*, 5547−5551.
(52) Lu, P.; Harris, S. J. Lithium Transport within the Solid Electrolyte Interphase. *Electrochem. Commun.* **2011**, *13*, 1035−1037.
(53) Lu, P.; Li, C.; Schneider, E. W.; Harris, S. J. Chemistry, Impedance, and Morphology Evolution in Solid Electrolyte Interphase Films during Formation in Lithium Ion Batteries. *J. Phys. Chem. C* **2014**, *118*, 896−903.
(54) Verma, P.; Maire, P.; Novák, P. A Review of the Features and Analyses of the Solid Electrolyte Interphase in Li-Ion Batteries. *Electrochim. Acta* **2010**, *55*, 6332−6341.
(55) Harris, S.; Lu, P. Effects of Inhomogeneities - Nanoscale to Mesoscale - on the Durability of Li-Ion Batteries. *J. Phys. Chem. C* **2013**, *117*, 6481−6492.
(56) McDowell, M. T.; Lee, S. W.; Harris, J. T.; Korgel, B. A.; Wang, C.; Nix, W. D.; Cui, Y. In Situ TEM of Two-Phase Lithiation of Amorphous Silicon Nanospheres. *Nano Lett.* **2013**, *13*, 758−764.
(57) Wang, J. W.; He, Y.; Fan, F.; Liu, X. H.; Xia, S.; Liu, Y.; Harris, C. T.; Li, H.; Huang, J. Y.; Mao, S. X.; et al. Two-Phase Electrochemical Lithiation in Amorphous Silicon. *Nano Lett.* **2013**, *13*, 709−715.
(58) Zhang, S. S.; Xu, K.; Jow, T. R. EIS Study on the Formation of Solid Electrolyte Interface in Li-Ion Battery. *Electrochim. Acta* **2006**, *51*, 1636−1640.
(59) Zhang, S.; Ding, M. S.; Xu, K.; Allen, J.; Jow, T. R. Understanding Solid Electrolyte Interface Film Formation on Graphite Electrodes. *Electrochem. Solid-State Lett.* **2001**, *4*, A206−A208.
(60) Pinson, M. B.; Bazant, M. Z. Theory of SEI Formation in Rechargeable Batteries: Capacity Fade, Accelerated Aging and Lifetime Prediction. *J. Electrochem. Soc.* **2012**, *160*, A243−A250.

(61) Smith, A. J.; Burns, J. C.; Zhao, X.; Xiong, D.; Dahn, J. R. A High Precision Coulometry Study of the SEI Growth in Li/Graphite Cells. *J. Electrochem. Soc.* **2011**, *158*, A447.
(62) Zhao, K.; Pharr, M.; Hartle, L.; Vlassak, J. J.; Suo, Z. Fracture and Debonding in Lithium-Ion Batteries with Electrodes of Hollow Core−shell Nanostructures. *J. Power Sources* **2012**, *218*, 6−14.
(63) Freund, L. B.; Suresh, S. *Thin Film Materials: Stress, Defect Formation and Surface Evolution*, 1st ed.; Cambridge University Press: New York, 2003.
(64) Ashby, M. F. *Materials Selection in Mechanical Design*, 4th ed.; Butterworth-Heinemann: Oxford, 2011; pp 57−96.
(65) Tokranov, A.; Sheldon, B. W.; Lu, P.; Xiao, X.; Mukhopadhyay, A. The Origin of Stress in the Solid Electrolyte Interphase on Carbon Electrodes for Li Ion Batteries. *J. Electrochem. Soc.* **2013**, *161*, A58−A65.